

# A Simple Family of Models for Eccentric Keplerian Fluid Disks

Thomas S. Statler

*Department of Physics and Astronomy, 251B Clippinger Research Laboratories, Ohio University, Athens,  
OH 45701, USA*

[statler@ohio.edu](mailto:statler@ohio.edu)

## ABSTRACT

In order to be in a long-lived configuration, the density in a fluid disk should be constant along streamlines to prevent compressional ( $PdV$ ) work from being done cyclically around every orbit. In a pure Kepler potential, flow along aligned, elliptical streamlines of constant eccentricity will satisfy this condition. For most density profiles, differential precession driven by the pressure gradient will destroy the alignment; however, in the razor-thin approximation there is a family of simple equilibria in which the precession frequency is the same at all radii. These disks may therefore be long-lived at significant eccentricities. The density can be made axisymmetric as  $r \rightarrow 0$ , while maintaining the precession rate, by relaxing the requirement of constancy along streamlines in an arbitrarily small transition region near the center. In the limit of small eccentricity, the models can be seen as acoustically perturbed axisymmetric disks, and the precession rate is shown to agree with linear theory. The perturbation is a traveling wave similar to an ocean wave, with the fluid rising and falling epicyclically in the gravitational field of the central mass. The expected emission line profiles from the eccentric disks are shown to be strongly asymmetric in general, and, in extreme cases, prone to misinterpretation as single narrow lines with significant velocity offsets.

*Subject headings:* galaxies: kinematics and dynamics—galaxies: nuclei—galaxies: structure—stars: formation—stars: novae, cataclysmic variables

## 1. Introduction

Accretion disks, protostellar disks, and galactic disks are almost always assumed to be axisymmetric or nearly so. This assumption is not without justification. Disks support a rich spectrum of stable and unstable modes which can efficiently redistribute angular momentum while viscous, collisional, and radiative processes dissipate energy. Circularization is then a naturally expected result. Nonetheless, disks of finite eccentricity may play an important role in certain astrophysical systems, and, indeed, appear to be required by observed phenomena on scales from AU to parsecs.

Two examples illustrate this need particularly well. At the stellar scale, eccentric disks are well established as the source of the superhump phenomenon in short-period cataclysmic variables. The period of these transient luminosity variations differs by a few percent from the binary orbital period, and the difference is readily explained by a precession of the disk (Vogt 1982; Osaki 1985). The eccentricity is “pumped” by the binary tidal field; numerical and analytic studies (Whitehurst 1988; Lubow 1991) indicate that the

eccentricity can be excited at the 3:1 Lindblad resonance (but see Heemskerk (1994) and Stehle (1999) for dissenting views). While the eccentricity may vary between outbursts, the repeatability of superhump light curves within an outburst (Patterson 1998) indicates that the eccentricity is not washed away on short time scales by differential precession. Instead, the disk needs to precess coherently for at least several orbital periods. The primary driver for this precession is most likely the gravity of the secondary star, but the disk’s own pressure gradient may also be a significant influence (Murray 2000).

At the parsec scale, the best studied eccentric disk candidate is the “double nucleus” of M31 (Lauer et al. 1993; Tremaine 1995; Kormendy & Bender 1999). This disk is stellar rather than gaseous, and is essentially isolated in the Keplerian potential of the central black hole, since neither the bulge nor the main disk has significant influence at this scale. Assuming the disk is not a transient, its structure must be such that its own self gravity is able to drive a coherent precession. This condition imposes a characteristic non-monotonic radial eccentricity profile on the disk (Statler 1999; Salow & Statler 2001), which is reproduced by dynamical simulations (Bacon et al. 2001). However, whether the eccentricity can be self-excited or must be tidally driven remains at issue (Bacon et al. 2001; Tremaine 2001), and the dynamical stability of such configurations is undetermined.

This paper takes up a question complementary to both of the above examples, namely, whether isolated Keplerian fluid disks can exist in long-lived eccentric equilibria. I will not address directly issues of hydrodynamic stability, which are extremely complex—even in axisymmetric systems—and far beyond the simple arguments presented here. But some necessary constraints on disk structure can be gleaned without a lengthy stability analysis. A slowly evolving disk should have a density that is approximately constant around streamlines. Were this not the case,  $PdV$  work would be done cyclically, and most likely irreversibly, around every orbit, dissipating the eccentric motions. In addition, the density and pressure must be such that perturbed streamlines can precess coherently. In the approximation of a razor-thin two dimensional disk with a polytropic equation of state and negligible mass, these minimal criteria for astrophysical realism are sufficient to define a remarkably simple family of eccentric disk models.

The arguments of the paper are laid out as follows: Section 2 presents the basic properties of the models. Simple scaling arguments are used in § 2.1 to derive the radial density profile for an assumed equation of state. Section 2.2 calculates the pressure-driven precession, and demonstrates that in the frame that rotates at the precession frequency, the motion of fluid elements is Keplerian to first order in the pressure. In § 2.3 the slightly sticky question of the inner boundary condition is considered. It is shown how the central eccentricity can be taken smoothly to zero by altering the density profile in an arbitrarily small transition region. The structure of the models in the low-eccentricity limit is shown in § 3 to correspond to that of axisymmetric disks perturbed by an  $m = 1$  traveling wave. The expected emission-line profiles from unresolved disks are computed in § 4. Finally, § 5 discusses the connection with other work on eccentric disks, describes the possible instabilities that could affect the models, and reiterates the main results.

## 2. Disk Models

### 2.1. Scaling Arguments and Radial Profile

The disks of this paper are assumed to be planar and razor-thin, with zero thickness perpendicular to the plane. The fluid has zero viscosity, and is characterized by a surface density  $\Sigma$  and a two-dimensional

pressure  $\Pi$ , related by a 2-D analogue of a polytropic equation of state,

$$\Pi = K\Sigma^{1+1/n}, \quad (1)$$

in which  $n$  is the polytropic index. Sound waves travel at a speed

$$c = \left[ \left( \frac{n+1}{n} \right) \frac{\Pi}{\Sigma} \right]^{1/2}, \quad (2)$$

and a fluid element feels a force<sup>1</sup>  $-\nabla\Pi/\Sigma$  in the presence of a pressure gradient. The force can also be written as the negative gradient of the enthalpy  $H$ , where

$$H = K(n+1)\Sigma^{1/n}. \quad (3)$$

The gravity of the disk is ignored.

A disk of non-interacting particles (or pressure-free fluid elements) on aligned Kepler orbits has a surface density given by (Statler 1999)

$$\Sigma(a, E) = \frac{\mu(a)}{2\pi a} \frac{(1-e^2)^{1/2}}{1-e^2 - ae'(e+\cos E)}. \quad (4)$$

In equation (4),  $a$  is the semimajor axis and  $E$  is the eccentric anomaly. The arbitrary function  $\mu(a)$  gives the mass per unit interval of  $a$ , and the eccentricity profile is described by  $e(a)$  and its first derivative  $e'(a)$ . Equation (4) is valid only if the orbits do not cross, which requires  $|e+ae'| < 1$ ; but  $e$  is *not* assumed to be small. (A more general version of this formula for unaligned orbits is given in Appendix A.)

Clearly if  $e' = 0$ , then  $\Sigma = \Sigma(a)$  and the density is constant around each orbit. This happens because the speed at each point around the orbit is inversely proportional to the local separation between neighboring orbits, and so competing terms in the equation of continuity cancel. Now, treating the pressure as a perturbation, the equation of state (1) implies that the pressure is stratified on the unperturbed orbits. The perturbing force on each fluid element is therefore perpendicular to the orbit, and does no work. Its primary effect is to drive a precession, at a rate  $\Omega_p$  which must be constant at all radii for the disk to be long-lived at finite eccentricity. This requirement is sufficient to determine the radial density profile of the disk, as follows: The small dimensionless parameter in the problem is  $\epsilon = \Omega_p/\omega$ , where  $\omega$  is the Keplerian mean motion. Since the latter scales as  $a^{-3/2}$ ,  $\Omega_p = \text{constant}$  implies  $\epsilon \sim a^{3/2}$ . To leading order,  $\epsilon$  must be proportional to the ratio of the perturbing force  $-\nabla\Pi/\Sigma$  to the Keplerian force  $GM_c/r^2$ , where  $M_c$  is the central mass. These quantities should each be thought of as averaged over the unperturbed orbit; since  $e = \text{constant}$ , these averages are proportional to  $-(d\Pi/da)/\Sigma$  and  $GM_c/a^2$ , respectively. The required scaling for  $\epsilon$  then implies that  $(d\Pi/da)/\Sigma \sim a^{-1/2}$ , which can be written as

$$K \left( 1 + \frac{1}{n} \right) \Sigma^{-1+1/n} d\Sigma = - \left( \frac{a}{a_*} \right)^{-1/2} da, \quad (5)$$

where  $a_*$  is an arbitrary constant. Integrating this equation and defining  $a_1 \equiv [K(n+1)/2(n-1)]^2 a_*$  gives the density profile

$$\Sigma(a) = \Sigma_0 \left[ 1 - (a/a_1)^{1/2} \right]^n, \quad (6)$$

---

<sup>1</sup>Throughout this paper “force” refers to force per unit mass.

where the surface density is equal to  $\Sigma_0$  at the center and falls to zero at  $a = a_1$ .

In the limit  $n \rightarrow \infty$  the equation of state (1) becomes isothermal and one obtains the density law

$$\Sigma = \Sigma_0 \exp \left[ -(a/h)^{1/2} \right], \quad (7)$$

where  $h$  is a constant scale length. However, this disk is infinite in extent, requiring  $\epsilon$  to become arbitrarily large since it must scale as  $a^{3/2}$ . I therefore exclude the isothermal case as unphysical.

## 2.2. Precession Rate and Surface Density

Fluid elements in the disk move along perturbed Kepler orbits. Ordinarily one would expect, in addition to the secular precession, cyclic variations in the orbital elements that would distort the pure ellipses and necessitate a first order correction to the surface density. In this case, however, one can show that the correction is zero.

Using equations (2), (3), and (6), the enthalpy can be written as

$$H = nc_0^2 \left[ 1 - (a/a_1)^{1/2} \right], \quad (8)$$

where  $c_0$  is the sound speed at  $a = 0$ . The radial and tangential components,  $\bar{R}$  and  $\bar{T}$ , of the perturbing force are therefore given by

$$\begin{aligned} (\bar{R}, \bar{T}) &= -\frac{dH}{da} \left( \frac{\partial a}{\partial r}, \frac{1}{r} \frac{\partial a}{\partial f} \right) \\ &= \frac{nc_0^2}{2(1-e^2)(aa_1)^{1/2}} (1 + e \cos f, -e \sin f), \end{aligned} \quad (9)$$

where  $f$  is the true anomaly and  $a = r(1 + e \cos f)/(1 - e^2)$ . But the Keplerian velocity has components

$$(v_R, v_T) = \frac{(GM_c)^{1/2}}{a^{1/2}(1-e^2)^{1/2}} (e \sin f, 1 + e \cos f); \quad (10)$$

consequently, in the frame that rotates at speed  $\Omega_p$ , the Coriolis term  $-2\Omega_p \hat{z} \times \mathbf{v}$  will identically cancel the pressure gradient if

$$\Omega_p = -\frac{nc_0^2}{4[GM_c a_1 (1-e^2)]^{1/2}}. \quad (11)$$

In this case, the disk is globally in *geostrophic balance*, and the only force term surviving in the Euler equation is the Kepler term  $-GM_c/r^2$ . (The centrifugal term  $\Omega_p^2 r$  is second order.) Thus *in the rotating frame* the fluid elements follow exact Kepler ellipses, and the surface density is given by equation (6) with no first-order correction.

It is easy to see intuitively why this result holds. Since the density is constant around each orbit, the perturbing force is proportional to the pressure gradient, which is inversely proportional to the separation between isobars. But the isobars are the orbits, whose separation is inversely proportional to the orbital speed when  $e = \text{constant}$ . Thus the perturbing force is both proportional to the velocity in magnitude and perpendicular to it in direction, just as the Coriolis force is. The two forces can cancel on all orbits for the *same*  $\Omega_p$  owing to the  $a^{1/2}$  dependence of the enthalpy.

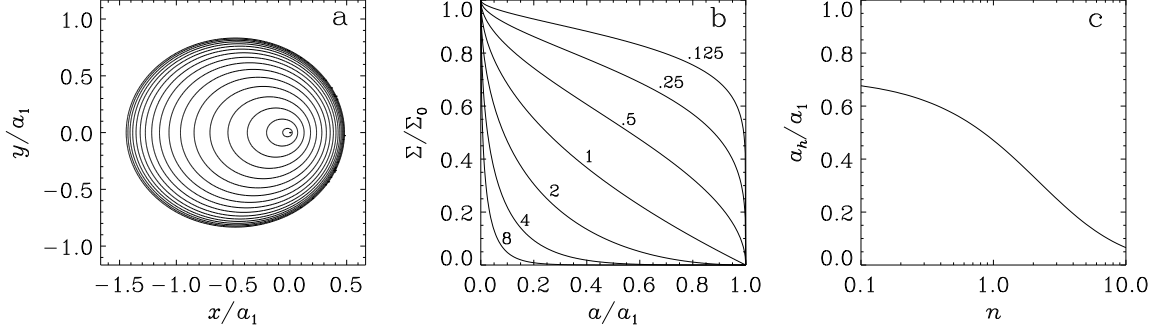


Fig. 1.— (a) Surface density contours for the disk with  $n = 3$  and  $e = 0.5$ . Contours are logarithmically spaced by factors of 2. (b) Surface density as a function of semimajor axis for models with values of the polytropic index  $n$  as indicated. (c) Semimajor axis enclosing half the mass as a function of  $n$ .

One can verify that equation (11) agrees with the precession rate obtained from standard perturbation theory by using equation (9) in the formula for the instantaneous drift rate of the argument of pericenter,

$$\dot{\varpi} = \frac{1}{e} \left[ \frac{a(1-e^2)}{GM_c} \right]^{1/2} \left( -\bar{R} \cos f + \bar{T} \sin f \frac{2+e \cos f}{1+e \cos f} \right) \quad (12)$$

(Burns 1976; Murray & Dermott 1999), and averaging around the orbit. Equation (11) may also be written in the form

$$\Omega_p = -\frac{n}{4(1-e^2)^{1/2}} \left( \frac{c_0}{v_1} \right)^2 \omega_1, \quad (13)$$

where  $v_1$  and  $\omega_1$  are the Keplerian speed and mean motion at the disk edge. This shows that the expansion parameter  $\epsilon$  is basically  $a^{3/2}$  times the square of the ratio of the central sound speed to the edge Keplerian speed. Notice also that the precession is retrograde, and is faster for larger eccentricities.

Figure 1a shows a density contour plot for a disk with  $n = 3$  and  $e = 0.5$ , illustrating the stratification of the density on orbits. Figure 1b compares the radial density profiles for selected values of the index  $n$ . The total mass of the disk is

$$M = 24\pi \frac{\Gamma(n+1)}{\Gamma(n+5)} (1-e^2)^{1/2} \Sigma_0 a_1^2, \quad (14)$$

where  $\Gamma(x)$  denotes the gamma function. The semimajor axis  $a_h$  enclosing half the mass is given by the solution of

$$I_z(4, n+1) = \frac{1}{2}, \quad (15)$$

where  $I_x(p, q)$  is the incomplete beta function and  $z \equiv (a_h/a_1)^{1/2}$ . Figure 1c shows the variation of  $a_h$  with  $n$ . For  $n = 0$  the density is constant and  $a_h = 2^{-1/2} a_1$ ; as  $n$  increases the disks become increasingly centrally concentrated.

### 2.3. Behavior at the Center

The behavior of the models near their centers presents a problem. It is not realistic to expect  $e$  to remain finite as  $a \rightarrow 0$ , since there are no strongly eccentric central masses in astrophysical systems. One

could imagine carving out an inner hole from the disk to avoid the center; but this expedient would remove the pressure gradient needed to synchronize the precession of the innermost material with that of the rest of the disk. Instead, the eccentricity needs to go smoothly to zero at the center—or at small finite radii—while maintaining the precession rate. I show here how this transition may be effected by allowing the density to deviate from that in equation (6) over a small interval of  $a$ , in the approximation where the density and eccentricity changes are both small (in a sense defined below). Formally this assumption limits the treatment to eccentricities  $\lesssim 0.3$ ; but it seems reasonable that a similar approach can be taken for larger  $e$ .

Readers more interested in the results than in the technical details are invited to skip down to the last paragraph of this section.

At leading order, the changes to the precession frequency from the altered density and eccentricity profiles can be considered separately and summed. I begin with the former, replacing the surface density  $\Sigma$  by  $\Sigma[1 + \delta(a)]$ , where  $\delta$  is the fractional density increase. The equation of state gives

$$\frac{\nabla\Pi}{\Sigma} = \left(\frac{\nabla\Pi}{\Sigma}\right)_{\delta=0} + \frac{\delta}{n} \left(\frac{\nabla\Pi}{\Sigma}\right)_{\delta=0} + K(1+n^{-1})\Sigma_{\delta=0}^{1/n} \nabla\delta, \quad (16)$$

where, from equations (3) and (8),  $K = [n/(n+1)]c_0^2\Sigma_0^{-1/n}$ . The first term on the right-hand side is responsible for the precession given in equation (11). Because  $\delta$  is constant on orbits, the second term simply contributes an additional  $\delta/n$  times the same rate. The third term is more difficult. The radial and tangential components of  $\nabla\delta$  are

$$\frac{\partial\delta}{\partial r} = \delta' \frac{1+e\cos f}{1-e^2}, \quad \frac{1}{r} \frac{\partial\delta}{\partial f} = -\delta' \frac{e\sin f}{1-e^2}, \quad (17)$$

where  $\delta' \equiv d\delta/da$ . Using equations (6), (16), and the relations

$$\cos f = \frac{\cos E - e}{1 - e\cos E}, \quad \sin f = \frac{(1 - e^2)^{1/2} \sin E}{1 - e\cos E}, \quad (18)$$

this results in the force components

$$(\bar{R}, \bar{T}) = c_0^2 \left[ 1 - (a/a_1)^{1/2} \right] \delta' \left[ -\frac{1}{1 - e\cos E}, \frac{\sin E}{(1 - e^2)^{1/2}(1 - e\cos E)} \right]. \quad (19)$$

The instantaneous precession rate can be obtained from equation (12), written in terms of the eccentric anomaly using equation (18). Because  $\omega dt = (1 - e\cos E)dE$ , the resulting expression can be time-averaged around the orbit by multiplying by  $(1 - e\cos E)$  and averaging over  $E$ . (Useful formulae for evaluating the necessary averages are given in Appendix B.) Adding the contributions of both the second and third terms in equation (16), the total extra precession induced by the density enhancement  $\delta$  is found to be

$$\begin{aligned} \Omega_{p\delta} &= -\frac{c_0^2}{2[GMc_a(1-e^2)]^{1/2}} \\ &\times \left\{ \frac{\delta}{2} - \frac{\delta'[(aa_1)^{1/2} - a]}{e} \left[ 1 + 2\frac{(1-e^2)(1-e)(1-[1-e^2]^{1/2})}{e^2} \right] \right\}. \end{aligned} \quad (20)$$

Note that  $\Omega_{p\delta} < 0$  for positive density enhancements that diminish outward.

To calculate the corresponding result for the eccentricity gradient,  $\Sigma$  is replaced by  $\Sigma[1 + g(r, f)]$ , where, from equation (4),

$$g(r, f) = e'r \frac{2e + (1 + e^2)\cos f}{(1 - e^2)^2}. \quad (21)$$

The equation of state gives, to leading order in  $g$ ,

$$\frac{\nabla\Pi}{\Sigma} = \left( \frac{\nabla\Pi}{\Sigma} \right)_{e'=0} + \frac{g}{n} \left( \frac{\nabla\Pi}{\Sigma} \right)_{e'=0} + K(1+n^{-1})\Sigma_{e'=0}^{1/n} \nabla g. \quad (22)$$

As in equation (16), the first term on the right hand side gives the ordinary precession rate (11). However, the second term does not produce a proportional contribution because  $g$  is not constant around the orbit. Instead, it produces the force components

$$(\bar{R}, \bar{T}) = \frac{c_0^2}{2} \left( \frac{a}{a_1} \right)^{1/2} \frac{e'}{1-e^2} \left[ \frac{\cos E + e}{1-e \cos E}, -\frac{e \sin E (\cos E + e)}{(1-e^2)^{1/2}(1-e \cos E)} \right]. \quad (23)$$

The third term is algebraically cumbersome because of the gradient of  $g(r, f)$ . Defining

$$g_1(a) = e(e' + ae'') + 2a \frac{1+e^2}{1-e^2} e'^2, \quad (24a)$$

$$g_2(a) = e' + ae'' + \frac{4ae'^2}{1-e^2}, \quad (24b)$$

$$g_3(a) = eg_1(a) + e', \quad (24c)$$

$$g_4(a) = e[g_2(a) - e'], \quad (24d)$$

the components of  $\nabla g$  can be written as

$$\frac{\partial g}{\partial r} = \frac{g_1(a) + g_2(a) \cos E}{(1-e^2)(1-e \cos E)}, \quad \frac{1}{r} \frac{\partial g}{\partial f} = -\frac{[g_3(a) + g_4(a) \cos E] \sin E}{(1-e^2)^{3/2}(1-e \cos E)}. \quad (25)$$

This produces the force components

$$(\bar{R}, \bar{T}) = c_0^2 \left[ 1 - (a/a_1)^{1/2} \right] \frac{e'}{1-e^2} \left\{ -\frac{g_1(a) + g_2(a) \cos E}{1-e \cos E}, \frac{[g_3(a) + g_4(a) \cos E] \sin E}{(1-e^2)^{1/2}(1-e \cos E)} \right\}. \quad (26)$$

Following the same procedure as above, I find the total extra precession induced by the eccentricity gradient to be

$$\Omega_{pe'} = \frac{c_0^2}{(GM_{ca_1})^{1/2}} \frac{1}{e(1-e^2)^{3/2}} \left[ -\frac{ae'}{4} + \frac{(aa_1)^{1/2} - a}{e^2} \sum_{i=1}^4 c_i(a) g_i(a) \right], \quad (27)$$

where the  $c_i$  coefficients are given by

$$c_1(a) = -e(1-e^2) \left[ 1 - (1-e^2)^{1/2} \right], \quad (28a)$$

$$c_2(a) = (1-e^2)^{3/2} \left[ 1 - (1-e^2)^{1/2} \right], \quad (28b)$$

$$c_3(a) = 1 - \frac{e^2}{2} - (1-e^2)^{3/2}, \quad (28c)$$

$$c_4(a) = \frac{1-e^2}{e} \left[ 1 - \frac{e^2}{2} - (1-e^2)^{1/2} \right]. \quad (28d)$$

The inner transition region, where  $e$  is varying and  $\delta$  is nonzero, should join smoothly onto the main body of the disk, where  $e = e_0 = \text{constant}$ . The requirement that both regions precess together is given by

$$\Omega_p + \Omega_{p\delta} + \Omega_{pe'} = \Omega_{p0}, \quad (29)$$

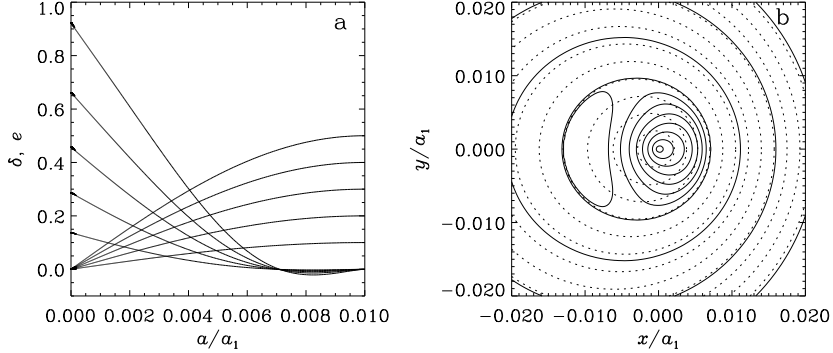


Fig. 2.— (a) Eccentricity  $e$  (thin lines) and fractional density enhancement  $\delta$  (thick lines) in the small inner region where  $e$  goes to zero according to equation (31), for models with  $n = 3$ . Successive curves, bottom to top, show results for main-body ellipticities  $e_0 = 0.1, 0.2, 0.3, 0.4, 0.5$ . (b) Surface density contours (solid lines) in the inner region of the model with  $n = 3$  and  $e_0 = 0.3$ . Contours are logarithmically spaced by factors of  $2^{1/8}$ . Dotted lines show representative fluid streamlines.

where  $\Omega_{p0}$  is the main body precession rate, i.e., equation (11) evaluated at  $e = e_0$ . This requirement yields a differential equation linking  $e(a)$  and  $\delta(a)$ :

$$\begin{aligned} \frac{2\delta'}{e^3}[(aa_1)^{1/2} - a] & \left\{ e^2 + 2(1 - e^2)(1 - e)[1 - (1 - e^2)^{1/2}] \right\} \\ & = \delta + n \left[ \left( \frac{1 - e^2}{1 - e_0^2} \right)^{1/2} - 1 \right] + \frac{1}{e(1 - e^2)} \left[ -ae' + 4 \frac{(aa_1)^{1/2} - a}{e^2} \sum_{i=1}^4 c_i(a)g_i(a) \right]. \end{aligned} \quad (30)$$

Since the point of the exercise is to manipulate  $e$ , I let  $e(a)$  be a fixed function and use equation (30) to calculate  $\delta(a)$ . In order to avoid a discontinuity in the gradient of the surface density,  $e(a)$ ,  $e'(a)$ , and  $e''(a)$  should all be continuous at  $a = a_0$ . A function with the desired properties is

$$e(a) = \begin{cases} e_0 \left[ 1 + \left( 1 - \frac{a}{a_0} \right)^b \left( \sin \frac{\pi a}{2a_0} - 1 \right) \right] & , \quad a \leq a_0; \\ e_0 & , \quad a_0 < a \leq a_1. \end{cases} \quad (31)$$

For  $0 < b < 1$ ,  $e(a)$  is linear at small  $a$  and joins smoothly onto  $e = e_0$  at  $a = a_0$ .

Figure 2a shows profiles of  $e$  and the fractional density enhancement  $\delta$  in a transition region with radius  $a_0 = 0.01a_1$  and  $b = 1/2$ , for a set of disks with  $n = 3$  and various eccentricities  $e_0$ . The results are fairly insensitive to the value of  $n$ . One sees that the eccentricity can be made to go continuously to zero at the center by steepening the density profile through most of the transition region. Figure 2b shows density contours in the transition region for the disk with  $e_0 = 0.3$ . While the density is no longer constant along streamlines, the variation about the mean is in the worst case only  $\pm 20\%$ . For  $e_0 \gtrsim 0.3$ , the needed density enhancement becomes of order unity, which violates the assumption behind equation (16). The assumption that  $g(r, f)$  is also small requires that  $ae' \ll 1 - e$ , a condition that is consistent with, but more stringent than, that for the non-crossing of orbits. The choice of  $e(a)$  in equation (31) begins to violate this condition for  $e_0 \gtrsim 0.3$ . But these conditions are required only by the first-order expansion; a more careful treatment may be able to find similar remedies for larger  $e_0$ .

### 3. Connection with Axisymmetric Disks

For small  $e$ , the structure of the models can also be understood in terms of the acoustic modes of an axisymmetric disk. A formalism for dealing with such disturbances is given by Papaloizou & Savonije (1991) and Heemskerk, Papaloizou, & Savonije (1992, hereafter HPS). They start with a perturbation to the surface density of the form

$$\Sigma = \Sigma(r) + \Sigma'(r)e^{i(m\phi+\sigma t)}, \quad (32)$$

where  $\Sigma(r)$  refers to the unperturbed disk; similar forms are assumed for the other hydrodynamic quantities. They then merge the linearized fluid equations into a single operator equation (HPS's eqs. [9] and [10]):

$$\Sigma' = \mathcal{L}(W), \quad (33a)$$

where

$$\begin{aligned} \mathcal{L}(W) &\equiv -\frac{1}{r} \frac{d}{dr} \left( \frac{r\Sigma}{D} \left[ \frac{dW}{dr} + \frac{2m\Omega\bar{\sigma}W}{\kappa^2 r} \right] \right) \\ &\quad + \left[ \frac{dW}{dr} + \frac{2m\Omega\bar{\sigma}W}{\kappa^2 r} \right] \frac{2m\Omega\bar{\sigma}\Sigma}{\kappa^2 r D} + \frac{mW}{\bar{\sigma}r} \frac{d}{dr} \left( \frac{1}{\zeta} \right) - \frac{4m^2\Omega^2\Sigma W}{\kappa^4 r^2}, \end{aligned} \quad (33b)$$

$$\kappa^2 \equiv \frac{2\Omega}{r} \frac{d(r^2\Omega)}{dr}, \quad (33c)$$

$$\zeta \equiv \frac{1}{r\Sigma} \frac{d(r^2\Omega)}{dr}, \quad (33d)$$

$$\bar{\sigma} \equiv \sigma + m\Omega, \quad (33e)$$

$$D \equiv \bar{\sigma}^2 - \kappa^2, \quad (33f)$$

and  $\Omega$  is the circular frequency. In the simple case where the only gravity is that of the central mass,  $W = c^2\Sigma'/\Sigma$ , and equation (33) (rather than HPS's more complicated equation [15]) governs the modes.

In the axisymmetric limit, the present models have a surface density given by

$$\Sigma(r) = \Sigma_0 \left[ 1 - (r/a_1)^{1/2} \right]^n \quad (34)$$

and a sound speed given by

$$c^2(r) = c_0^2 \left[ 1 - (r/a_1)^{1/2} \right]. \quad (35)$$

The pressure gradient reduces  $\Omega$  from its Keplerian value to

$$\Omega = \left( \frac{GM_c}{r^3} \right)^{1/2} - \frac{nc_0^2}{4(GM_c a_1)^{1/2}}. \quad (36)$$

The difference in surface density between the eccentric and axisymmetric disks is, in the limit of small  $e$ ,

$$\Delta\Sigma = \Sigma_0 \left\{ \left[ 1 - (r/a_1)^{1/2} \left( 1 - \frac{e}{2} \cos f \right) \right]^n - \left[ 1 - (r/a_1)^{1/2} \right]^n \right\}. \quad (37)$$

For arbitrary  $n$ ,  $\Delta\Sigma$  is a superposition of Fourier harmonics. I restrict the discussion here to the case  $n = 1$ , so that

$$\Delta\Sigma = -\frac{\Sigma_0 e}{2} \left( \frac{r}{a_1} \right)^{1/2} \cos f. \quad (38)$$

This corresponds to a single  $m = 1$  term, with

$$\Sigma' = \frac{\Sigma_0 e}{2} \left( \frac{r}{a_1} \right)^{1/2}, \quad (39)$$

and consequently

$$W = \frac{c_0^2 e}{2} \left( \frac{r}{a_1} \right)^{1/2}. \quad (40)$$

Direct substitution into equation (33b) shows, after lengthy algebra, that equation (33a) is satisfied to leading order in  $c_0^2$  when  $\sigma = c_0^2/[4(GM_c a_1)^{1/2}]$ . The form of the exponential in equation (32) indicates that this value corresponds to a *regression* of the pattern and agrees with equation (11) for  $n = 1$  and  $e = 0$ . Also, since  $\sigma$  is real, the mode is stable.

The reader may have noticed that the inner and outer radial boundary conditions have not played a role in this discussion. The fact that  $\Sigma'$  is real means that the mode has zero radial wavenumber. Unlike WKB waves, this wave is completely unwound and propagates only in the tangential direction. In this respect it is not really a “mode” in the sense of being a standing wave in a resonant cavity. Instead, it is a traveling wave. In fact, since the wave does not compress the fluid—even though the fluid itself is *not* incompressible—it bears a close similarity to an ocean wave. Like an ocean wave, fluid elements move epicyclically with respect to the mean flow, and the restoring force for the pressure driven vertical displacement is the gravity of the central mass. The variation of the sound speed and flow velocity with depth conspire to refract the wave around the central mass while keeping the wave front straight.

#### 4. Line Profiles

Constant-eccentricity Keplerian disks are kinematically simple. Spatially resolved rotation curves along any line through the central mass will show velocities proportional to  $r^{-1/2}$ , but will not, in general, be antisymmetric about the center. The observed velocities on opposite sides of the central mass will differ by a multiplicative factor depending on both the eccentricity and the viewing geometry. Kinematic measurements along several position angles would be necessary to determine the disk structure and orientation; but a reasonably accurate estimate of the central mass could be obtained by averaging the masses derived from each side of the rotation curve under the naive assumption of circular motion.

It seems more likely, however, that disks of the sort discussed here will usually be unresolved. The expected emission line profiles from an unresolved disk can be straightforwardly calculated. For simplicity, I assume the emission comes from a recombination line of a species whose density follows the total density, so that the emissivity is proportional to  $\Sigma^2$ . The disk is assumed to be optically thin with the line of sight in the disk plane, an angle  $\theta$  from the major axis. A mass  $dM$  on a single Kepler orbit in the disk produces a contribution to the line of sight velocity distribution (LOSVD)  $f(v_\ell)$  given by

$$df(v_\ell) = \frac{dM}{2\pi(GM_c/a)^{1/2}} \frac{(1 - e \cos E)^3}{(\cos E - e) \cos \theta + (1 - e^2)^{1/2} \sin E \sin \theta}. \quad (41)$$

At each  $v_\ell$ , the contribution must be summed over the two values of  $E$  given by

$$\sin E_1 = \frac{A - B(A^2 + B^2 - 1)^{1/2}}{A^2 + B^2}, \quad \cos E_1 = \frac{B + A(A^2 + B^2 - 1)^{1/2}}{A^2 + B^2}, \quad (42)$$

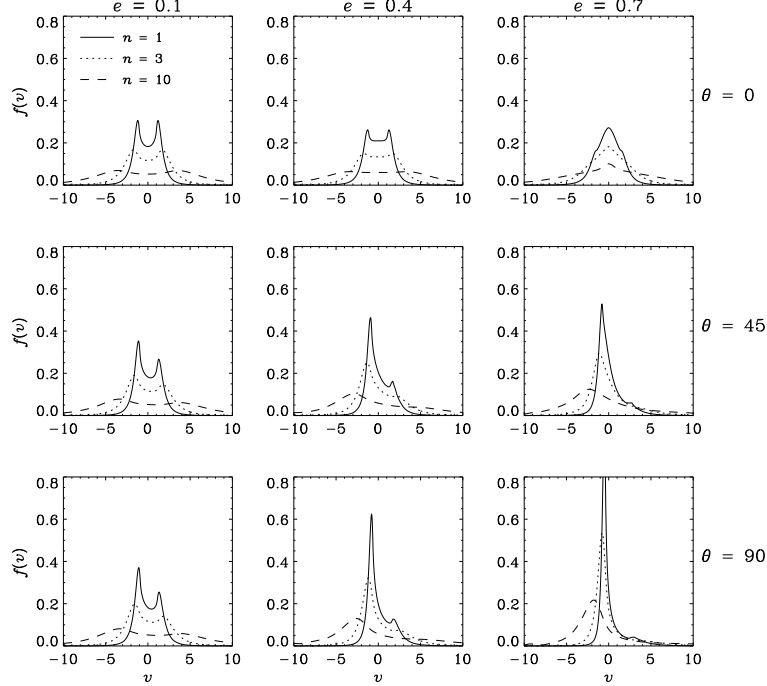


Fig. 3.— Simulated line profiles for unresolved elliptic disks. Relative fluxes per unit interval of velocity are shown for velocities in units of  $(GM_c/a_1)^{1/2}$ . Results for eccentricities of 0.1, 0.4, and 0.7 are shown in the first, second and third columns, and for lines of sight along, oblique to, and perpendicular to the disk major axis in the top, middle, and bottom rows. Different line styles correspond to values of the polytropic index  $n$  as indicated at top left. The central sound speed is 0.2.

and

$$\sin E_2 = \frac{A + B(A^2 + B^2 - 1)^{1/2}}{A^2 + B^2}, \quad \cos E_2 = \frac{B - A(A^2 + B^2 - 1)^{1/2}}{A^2 + B^2}, \quad (43)$$

where

$$A \equiv -\frac{(GM_c/a)^{1/2}}{v_\ell} \cos \theta, \quad (44a)$$

$$B \equiv \frac{(GM_c/a)^{1/2}}{v_\ell} (1 - e^2)^{1/2} \sin \theta + e. \quad (44b)$$

These expressions ignore the precession of the disk, which adds a slow, retrograde, solid-body component to the rotation; this effect is included in the examples shown below, but makes only a tiny difference to the results. Assuming an ideal gas, the equation of state and the density profile imply a one-dimensional thermal velocity dispersion

$$\sigma_{\text{th}}^2 = \frac{nc_0^2}{n+1} \left[ 1 - (a/a_1)^{1/2} \right]. \quad (45)$$

The LOSVD at each  $a$  is convolved to the thermal dispersion, and the results are integrated over the disk. No correction is made for a transition to  $e = 0$  at the center.

Line profiles for various models are shown in Figure 3. The line shape appears at first glance very sensitive to the polytropic index  $n$ . But much of this sensitivity is a simple scaling; for the same central

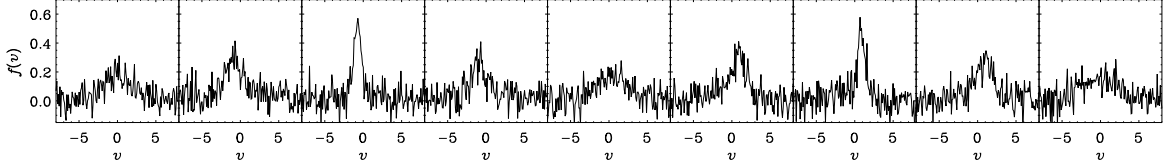


Fig. 4.— A sequence of line profiles for the  $n = 3$ ,  $e = 0.7$  model, shown (left to right) as the disk precesses through a complete period. Gaussian noise has been added to simulate observations. The true mean velocity is zero, but continuum misidentification could lead to spurious measurements of velocity offsets.

mass and limiting radius, disks of larger  $n$  show broader line profiles simply because they are more centrally concentrated. One also sees that the lines can be strongly asymmetric, even for eccentricities as small as 0.1. Where the profiles are double peaked, the stronger peak arises from the side of the disk containing the apocenters of the orbits, and consequently can appear at either positive or negative velocity. For eccentricities of 0.5 or larger, the secondary peak can disappear entirely. Even though the line centroid remains at zero velocity relative to the central mass, in the presence of noise the asymmetric primary peak could easily be mistaken for a single narrow line with a large velocity offset. Figure 4 shows a sequence of line profiles through a complete precession period for the  $n = 3$ ,  $e = 0.7$  disk, with noise added. In principle, the slow time evolution of the line profile could be detectable for some types of objects. For a cold protostellar disk, equation (11) implies a precession period of

$$T_p = 3900 C \left( \frac{M_c}{1 M_\odot} \right)^{1/2} \left( \frac{a_1}{100 \text{ AU}} \right)^{1/2} \left( \frac{c_0}{1 \text{ km s}^{-1}} \right)^{-2} \text{ yr}, \quad (46)$$

where the factor  $C \equiv (4/n)(1 - e^2)^{1/2}$  is of order unity. For a galactic nuclear disk,

$$T_p = 4 \times 10^7 C \left( \frac{M_c}{10^8 M_\odot} \right)^{1/2} \left( \frac{a_1}{1 \text{ pc}} \right)^{1/2} \left( \frac{c_0}{10 \text{ km s}^{-1}} \right)^{-2} \text{ yr}. \quad (47)$$

Offset or asymmetric emission lines are not uncommon in active galactic nuclei (AGN), but are usually qualitatively different from those shown above. Systematic offsets, e.g., of the [O III] line (Whittle 1985), are consistently toward the blue, and it is the line centroid, rather than the peak, that is shifted. Offsets of this sort should more naturally arise from outflows rather than orbital motion. AGN showing double-peaked lines characteristic of unresolved Keplerian motion may be modeled by axisymmetric relativistic disks when the blue peak is stronger than the red, the asymmetry arising from Doppler boosting (Chen, Halpern & Filippenko 1989). However, in a fraction of radio-loud AGN with disk-like H $\alpha$  emission, the red peak is stronger than the blue. Eracleous et al. (1995) appeal to eccentric disks to model these objects. Their models, like those presented here, have constant eccentricity, but the line emissivity is taken to be a function of  $r$  rather than  $a$ . Eracleous et al. (1995) consider general relativistic effects and estimate that differential relativistic precession would ruin the coherence of elliptic disks in AGN on timescales as short as decades, unless they were narrow rings. Bao et al. (1996) show that narrow rings can persist even in a strong field, and calculate the resulting line profiles. But it seems plausible that relativistic versions of the models of this paper could be found in which combined relativistic and hydrodynamic effects could drive a uniform precession, extending the lives of wide disks.

## 5. Discussion

I have presented the properties of a particularly simple family of idealized models for eccentric Keplerian fluid disks, in which the internal pressure gradient drives a coherent precession of the apses of the constant-eccentricity streamlines. In the frame that rotates with the precession frequency, the pressure gradient balances the Coriolis force; the disks are therefore in global geostrophic balance, and the fluid motion is Keplerian, to first order in the pressure, in the rotating frame.

In the limit of small eccentricity, the models can be viewed as perturbed axisymmetric disks, and their elliptic distortions interpreted as traveling acoustic waves. These waves are related to the “slow”  $m = 1$  modes examined by Tremaine (2001), but are not physically the same. The elliptic distortions have radial wavenumber  $k = 0$ , which is maintained by a continuous refraction of the waves around the center, and therefore owe their existence to the particular density profile of the disk. The disk’s self gravity, which creates the true standing waves studied by Tremaine, is ignored in the present case. Including finite disk gravity may restrict the slow acoustic waves to a limited range of radii and/or turn them into standing waves with  $k \neq 0$ .

One should keep in mind that these models are highly idealized, and neglect at least two important effects present in real disks. First, fluid elements in a three-dimensional disk will experience a varying vertical compression around every orbit, since the vertical ( $z$ ) component of the Kepler force near the disk plane is proportional to  $z/r^3$ . The fractional magnitude of the variation depends on the eccentricity and not on the disk thickness. Second, shear viscosity is known to be a controlling factor in true accretion disks, and is likely to affect the structure of larger-scale disks in galactic nuclei which may not be actively accreting.

Turbulent viscosity can arise from any of a number of local instabilities, the leading candidate being the magnetorotational instability (Balbus & Hawley 1991) when magnetic fields are present. Angular momentum is transported efficiently by magnetic torques, and the instability’s growth time is of order the orbital period. The instability will therefore affect the structure of any disk with even a weak magnetic field, as long as the ionization is sufficiently high that the flux is effectively frozen in the fluid. On the other hand, the instability may be suppressed in protostellar (Wardle 1999) or protoplanetary (Reyes-Ruiz 2001) disks of very low ionization.

A purely hydrodynamical instability unique to non-axisymmetric disks has been studied by Goodman and collaborators (Goodman 1993; Ryu & Goodman 1994; Ryu, Goodman, & Vishniac 1996). The “eccentric instability” is intimately connected with the inertial oscillations, force-free epicyclic motions supported by any rotating or shearing medium. Because the spectrum of the inertial oscillations is continuous, there is always a mode of the right frequency available to be parametrically amplified by a periodic disturbance, such as a traveling acoustic wave. The instability is intrinsically three-dimensional—the motions of the amplified mode are inclined to the disk plane—and therefore would affect any finite-thickness analogue of the present models.

Turbulence may also be associated with vortices, whose importance in disks is considered by Adams & Watkins (1995). They point out that, according to Kelvin’s circulation theorem, vorticity should not be spontaneously created when pressure and density contours coincide and the viscosity is zero. Thus the models, as defined here, should not be unstable to vortex generation. Real disks, however, may be radiatively heated by their central objects and radiatively cooled by line or continuum emission. The temperature could then vary significantly around streamlines, in which case vortices could be generated. A careful treatment of the radiative transfer within the models would be needed to determine if this is the case.

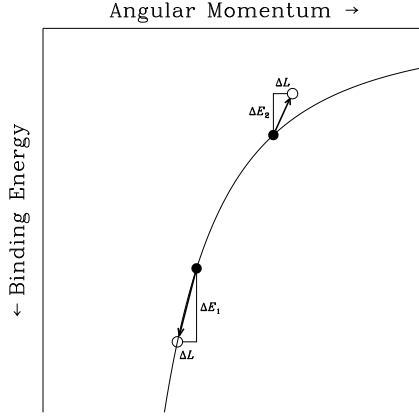


Fig. 5.— Illustrating why a circular disk is not the minimum energy configuration for a given angular momentum. A pair of circular rings (filled circles) is plotted in the Lindblad diagram for a Kepler potential. *Smooth curve* shows the circular orbits. *Open circles* show the rings displaced so as to conserve total angular momentum and lower the total energy ( $|\Delta E_2| < |\Delta E_1|$ ), leaving the outer ring eccentric.

It may be tempting to argue that viscous dissipation will naturally circularize any disk on the grounds that, at a fixed angular momentum, the circular configuration is the state of lowest energy. However, this latter statement is true only for single orbits, and does not apply to disks where energy and angular momentum can be traded between orbits. To illustrate, consider the toy problem of two circular rings of equal mass. Figure 5 shows a Lindblad diagram for this system, with both rings (filled circles) lying on the locus of circular orbits (smooth curve) for the Kepler potential. Now imagine shifting the inner ring to a more tightly bound circular orbit (lower open circle), lowering its energy by  $\Delta E_1$  and its angular momentum by  $\Delta L$ . Angular momentum can be conserved by depositing the same  $\Delta L$  in the outer ring, along with some amount of energy  $\Delta E_2$ . Because of the shape of the circular-orbit locus, however, the shifted outer ring (upper open circle) can move away from the circular orbits (i.e., can become eccentric) even if  $|\Delta E_2| < |\Delta E_1|$ . *Thus, for any circular disk, there is an eccentric disk with the same angular momentum and lower energy.*

Energy arguments alone are therefore not sufficient to determine whether eccentric disks can survive in the presence of shear viscosity. A number of more detailed calculations have been attempted, but the results are still ambiguous. An analytic and numerical study of the viscous evolution of pressure-free eccentric gas disks and streams by Syer & Clarke (1992) finds that the eccentricity nearly always *increases* or remains constant under the influence of viscous effects. This result is corroborated by the purely analytic work of Lyubarskij, Postnov, & Prokhorov (1994), who show that evolution at constant  $e$  is one of many possible paths for the disk. Ogilvie (2001) finds, in contrast, that with gas pressure included, eccentric motions dissipate on a viscous time scale. In three-dimensional smooth-particle hydrodynamic simulations (Mastrodemos & Morris 1998), broad, persistently eccentric disks are found to form spontaneously in accreting winds. A more careful analysis of the simulations would be needed to clarify the detailed structure of the disks and the role of pressure in maintaining them. Disks whose radial profiles are determined by accretion processes may not evolve toward the special profiles required by the models in this paper, and consequently may be unable to synchronize their precession rates and remain eccentric. But the appearance of long-lived eccentric disks in simulations where no special effort is made to create them suggests that Nature may have ways to make

similar disks in abundance.

The author is grateful for helpful insights and suggestions from Mike Eracleous, Glen Stewart, Joe Shields, Steve Balbus, and Larry Wilen. This work was supported by NSF CAREER grant AST-9703036.

### Appendix A. Surface Density of an Unaligned Keplerian Disk

Equation (4) can be generalized to an unaligned planar disk in which the eccentricity and longitude of pericenter are given by functions  $e(a)$  and  $\varpi(a)$  respectively. The result is

$$\Sigma(a, E) = \frac{\mu(a)}{2\pi a} \frac{(1 - e^2)^{1/2}}{1 - e^2 - a [e'(e + \cos E) + \varpi'e(1 - e^2)^{1/2} \sin E]}, \quad (48)$$

where the eccentric anomaly  $E$  is measured from pericenter on each orbit. Alternatively, one might prefer to have the surface density in terms of a fixed polar coordinate system  $(r, \phi)$ . In this case,

$$\Sigma(r, \phi) = \frac{\mu(a)}{2\pi a} \frac{(1 - e^2)^{1/2}}{1 - e^2 - e'[2ae + r \cos(\phi - \varpi)] - re\varpi' \sin(\phi - \varpi)}, \quad (49)$$

where  $a(r, \phi)$  can be found efficiently by iteration using the prescription

$$a_{j+1} = (1 - k)a_j + kr \frac{1 + re(a_j) \cos[\phi - \varpi(a_j)]}{1 - [e(a_j)]^2}. \quad (50)$$

Values of the relaxation factor  $k \approx 0.5$  usually give rapid convergence. The above results generalize the formulae of Borderies, Goldreich, & Tremaine (1986) to arbitrary eccentricity, but remain valid only when the criterion for non-crossing of orbits (Ogilvie 2001),

$$(e + ae')^2 + (ae\varpi')^2 < 1, \quad (51)$$

is satisfied.

### Appendix B. Helpful Integrals

The following integrals are useful in evaluating the average precession rates in Section 2.3:

$$\frac{1}{\pi} \int_0^\pi \frac{dE}{1 - e \cos E} = \frac{1}{(1 - e^2)^{1/2}}, \quad (52)$$

$$\frac{1}{\pi} \int_0^\pi \frac{\cos E dE}{1 - e \cos E} = \frac{1 - (1 - e^2)^{1/2}}{e(1 - e^2)^{1/2}}, \quad (53)$$

$$\frac{1}{\pi} \int_0^\pi \frac{\cos^2 E dE}{1 - e \cos E} = \frac{1 - (1 - e^2)^{1/2}}{e^2(1 - e^2)^{1/2}}, \quad (54)$$

$$\frac{1}{\pi} \int_0^\pi \frac{\sin^2 E dE}{1 - e \cos E} = \frac{1 - (1 - e^2)^{1/2}}{e^2}, \quad (55)$$

$$\frac{1}{\pi} \int_0^\pi \frac{\sin^2 E \cos E dE}{1 - e \cos E} = \frac{2 - e^2 - 2(1 - e^2)^{1/2}}{2e^3}, \quad (56)$$

$$\frac{1}{\pi} \int_0^\pi \frac{\sin^2 E \cos^2 E dE}{1 - e \cos E} = \frac{2 - e^2 - 2(1 - e^2)^{1/2}}{2e^4}. \quad (57)$$

## REFERENCES

Adams, F. C. & Watkins, R. 1995, *ApJ*, 451, 314

Bacon, R., Emsellem, E., Combes, F., Copin, Y., Monnet, G., & Martin, P. 2001, *A&A*, 371, 409

Balbus, S. & Hawley, J. 1991, *ApJ*, 376, 214

Bao, G., Hadrava, P., & Østgaard, E. 1996, *ApJ*, 464, 684

Borderies, N., Goldreich, P., & Tremaine, S. 1986, *Icarus*, 68, 522.

Burns, J. A. 1976, *Am. J. Phys.*, 44, 944

Chen, K., Halpern, J. P., & Filippenko, A. V. 1989, *ApJ*, 339, 742

Eracleous, M., Livio, M., Halpern, J. P., & Storchi-Bergmann, T. 1995, *ApJ*, 438, 610

Goodman, J. 1993, *ApJ*, 406, 596

Heemskerk, M. H. M. 1994, *A&A*, 288, 807

Heemskerk, M. H. M., Papaloizou, J. C., & Savonije, G. J. 1992, *A&A*, 260, 161 (HPS)

Kormendy, J., & Bender, R. 1999, *ApJ*, 522, 772

Lauer, T. R., Faber, S. M., Groth, E. J., Shaya, E. J., Campbell, B., Code, A., Currie, D. G., Baum, W. A., Ewald, S. P., Hester, J. J., Holtzman, J. A., Kristian, J., Light, R. M., & Westphal, J. A. 1993, *AJ*, 106, 1436

Lubow, S. 1991, *ApJ*, 381, 259

Lyubarskij, Yu. E., Postnov, K. A., & Prokhorov, M. E. 1994, *MNRAS*, 266, 583

Mastrodemos, N. & Morris, M. 1998, *ApJ*, 497, 303

Murray, J. R. 2000, *MNRAS*, 314, L1

Murray, C. D. & Dermott, S. F. 1999, *Solar System Dynamics*, (Cambridge Univ. Press)

Ogilvie, G. I. 2001, *MNRAS*, 325, 231

Osaki, Y. 1985, *A&A*, 144, 369

Papaloizou, J. C. & Savonije, G. J. 1991, *MNRAS*, 248, 353

Patterson, J. 1998, *PASP*, 110, 1132

Reyes-Ruiz, M. 2001, *ApJ*, 547, 465

Ryu, D. & Goodman, J. 1994, *ApJ*, 422, 269

Ryu, D., Goodman, J., & Vishniac, E. T. 1996, *ApJ*, 461, 805

Salow, R. M. & Statler, T. S. 2001, *ApJ*, 551, L49

Statler, T. S. 1999, *ApJ*, 524, L87

Stehle, R. 1999, MNRAS, 304, 687

Syer, D. & Clarke, C. J. 1992, MNRAS, 255, 92

Tremaine, S. 1995, AJ, 110, 628

Tremaine, S. D. 2001, AJ, 121, 1776

Vogt, N. 1982 ApJ, 252, 653

Wardle, M. 1999, MNRAS, 307, 849

Whitehurst, R. 1988, MNRAS, 232, 35

Whittle, M. 1985, MNRAS, 213, 1